PNAS RESEARCH ARTICLE | BIOCHEMISTRY

Conformation-specific synthetic intrabodies modulate mTOR signaling with subcellular spatial resolution

Kelly M. O'Leary[a], Tomasz Slezak[a], and Anthony A. Kossiakoff[a,b,1]

Edited by Natalie Ahn, University of Colorado Boulder, Boulder, CO; received November 25, 2024; accepted April 2, 2025

Subcellular compartmentalization is integral to the spatial regulation of mechanistic target of rapamycin (mTOR) signaling. However, the biological outputs associated with location-specific mTOR signaling events are poorly understood and challenging to decouple. Here, we engineered synthetic intracellular antibodies (intrabodies) that are capable of modulating mTOR signaling with genetically programmable spatial resolution. Epitope-directed phage display was exploited to generate high affinity synthetic antibody fragments (Fabs) against the FKBP12–Rapamycin binding site of mTOR (mTOR^{FRB}). We determined high-resolution crystal structures of two unique Fabs that discriminate distinct conformational states of mTOR^{FRB} through recognition of its substrate recruitment interface. By leveraging these conformation-specific binders as intracellular probes, we uncovered the structural basis for an allosteric mechanism governing mTOR complex 1 (mTORC1) stability mediated by subtle structural adjustments within mTOR^{FRB}. Furthermore, our results demonstrated that synthetic binders emulate natural substrates by employing divergent yet complementary hydrophobic residues at defined positions, underscoring the broad molecular recognition capability of mTOR^{FRB}. Intracellular signaling studies showed differential time-dependent inhibition of S6 kinase 1 and Akt phosphorylation by genetically encoded intrabodies, thus supporting a mechanism of inhibition analogous to the natural product rapamycin. Finally, we implemented a feasible approach to selectively modulate mTOR signaling in the nucleus through spatially programmed intrabody expression. These findings establish intrabodies as versatile tools for dissecting the conformational regulation of mTORC1 and should be useful to explore how location-specific mTOR signaling influences disease progression.

intrabody | mTOR | allosteric | spatial | inhibition

Significance

Elucidating subcellular mechanisms of protein kinase signaling remains challenging due to the lack of spatial precision by genetic knockdown or pharmacological approaches. Here, synthetic intracellular antibodies (intrabodies) were engineered as genetically encodable inhibitors of mechanistic target of rapamycin (mTOR) signaling. We demonstrate the versatility of intrabodies as conformational probes by uncovering an allosteric mechanism that regulates the stability of mTOR complex 1. Furthermore, we illustrate the feasibility of decoupling subcellular spatial mTOR networks through direct functional perturbations by cytosol- or nucleus-restricted intrabody expression. This work highlights the potential of synthetic intrabodies for investigating structural and spatial mechanisms of therapeutically relevant protein kinase networks.

Mechanistic target of rapamycin (mTOR) is a serine/threonine protein kinase that regulates cellular growth and metabolism through multifaceted signaling phenotypes in specific tissues, cell types, and subcellular compartments (1–4). mTOR serves as the catalytic subunit in two functionally distinct assemblies, mTOR complex 1 (mTORC1) and mTOR complex 2 (mTORC2) (5–7), which phosphorylate independent sets of substrates in response to nutrient and growth factor stimulation (8). Numerous studies have highlighted the robust therapeutic potential of systemic mTOR inhibition by the natural product rapamycin or ATP-competitive inhibitors in diverse model organisms (9–16). However, undesirable side effects or feedback loops resulting from on-target mTORC1/mTORC2 inhibition have limited the clinical efficacy of mTOR inhibitors for various diseases such as diabetes, cancer, neurodegenerative disorders, and metabolic syndromes (17–19). Nevertheless, the emerging concept that tissue-specific (20, 21) and subcellular (22, 23) mTOR signaling networks are functionally linked to distinct biological outputs represents a promising path forward to decouple favorable therapeutic effects from toxicities associated with systemic mTOR inhibition.

How the subcellular spatial regulation of mTOR signaling influences mechanistically diverse processes such as nutrient-specific signal transduction, macromolecular metabolism, or transcriptional regulation remains elusive (24). While canonical mTORC1 signaling occurs at the surface of lysosomes (25, 26), mTORC1 activity has also been reported at noncanonical locations such as the plasma membrane, mitochondria, and nucleus (27–29). In fact, recent studies have pointed to mTOR as a driver of prostate cancer aggressiveness by rewiring androgen-dependent transcriptional networks from inside the nucleus (30–34). Uncovering whether mTOR activity is functionally relevant inside the nucleus, and if so, whether nuclear mTOR is active toward a defined set of substrates could provide valuable mechanistic insight to improve current therapeutic strategies. However, shortcomings in techniques to execute functional mTOR perturbations with subcellular spatial resolution represent a key technological barrier to our understanding.

Author affiliations: [a]Department of Biochemistry and Molecular Biology, The University of Chicago, Chicago, IL 60637; and [b]Institute for Biophysical Dynamics, The University of Chicago, Chicago, IL 60637

Author contributions: K.M.O. and A.A.K. designed research; K.M.O. and T.S. performed research; K.M.O. contributed new reagents/analytic tools; K.M.O., T.S., and A.A.K. analyzed data; and K.M.O. and A.A.K. wrote the paper.

The authors declare no competing interest.

This article is a PNAS Direct Submission.

[1]To whom correspondence may be addressed. Email: koss@bsd.uchicago.edu.

This article contains supporting information online at https://www.pnas.org/lookup/suppl/doi:10.1073/pnas.2424679122/-/DCSupplemental.

Published June 9, 2025.

The current repertoire of mTOR inhibitors operates on a whole-cell basis by disrupting catalysis, substrate recruitment, or both (21, 35, 36). We envisioned that recapitulating the molecular mechanism of rapamycin, which directly blocks substrate recruitment, using intracellular antibodies (intrabodies) would enable us to capture its therapeutic profile while maintaining control over its location inside cells (37). Rapamycin inhibits mTOR by first forming a complex with FK506-binding protein of 12 kDa (FKBP12) and then sequestering the FKBP12–Rapamycin binding (FRB) domain of mTOR (mTOR^{FRB}) located next to the catalytic cleft (38). This interaction selectively inhibits the phosphorylation of specific mTOR substrates, though not all, owing to the mechanistic diversity underlying mTOR substrate recruitment (39–41). Structural studies demonstrated that mTOR^{FRB} docking of ribosomal protein S6 kinase 1 (S6K1) and proline-rich Akt substrate of 40 kDa (PRAS40) is a competitive mechanism for regulating mTORC1 activity and suggested that several other mTORC1 substrates may require mTOR^{FRB} docking for their phosphorylation as well (42, 43). Therefore, we exploited the power of phage display to generate epitope-directed synthetic antibody fragments (Fabs) (44, 45) against the rapamycin binding site as a straightforward route to modulate mTOR signaling genetically. Synthetic affinity reagents provide distinctive advantages over traditional gene knockdowns or small-molecule inhibitors, including feasible tuning of target activity, masking of functional sites, and spatiotemporal control (46–50). Furthermore, Fabs serve as superior crystallization chaperones (51), and conversion to single chain variable fragment (scFv) format enables simple genetic portability into living cells (52).

Here, we describe a general framework to modulate mTOR^{FRB}-mediated substrate recruitment in a rapamycin-like fashion using genetically encodable scFv-based intrabodies. Structural and functional studies of two conformation-specific intrabodies revealed molecular insight into the allosteric regulation of the mTORC1 architecture mediated through subtle conformational rearrangements in the mTOR^{FRB} domain. Furthermore, we effectively decoupled cytosolic mTOR signaling from nuclear mTOR signaling through location-specific intrabody-based functional perturbations, demonstrating that subcellular mTOR networks can indeed be manipulated independently. Together, this proof-of-concept study establishes an approach to decouple spatially restricted functions of the mTOR signaling network systematically.

Results

Engineered Synthetic Antibodies (sABs) Selectively Obstruct the mTOR^{FRB} Substrate Recruitment Site. The mTOR^{FRB} domain is a small (11 kDa) four-helix bundle that facilitates the entry of some mTORC1 substrates into the catalytic cleft (41, 42). sABs were designed to engage with and modulate the mTOR signaling pathway by exploiting this stable and functional domain. Recombinant SNAP-tagged human mTOR^{FRB} was purified, biotinylated, and used as a target for five rounds of phage display biopanning (Fig. 1*A*). The concentration of mTOR^{FRB} was incrementally reduced from 1 μM in the first round to 2 nM in the last round to apply stringent selection pressure while maintaining 1 μM nonbiotinylated SNAP in solution. Phage ELISA identified seven unique phage clones exhibiting selective binding against mTOR^{FRB} for further characterization (*SI Appendix*, Fig. S1 *A* and *B*). Based on a previously reported design (52), these clones were converted into scFv or "intrabody" format and tested for intracellular solubility in human Expi293F cells. All seven unique scFv constructs displayed detectable intracellular expression, albeit at varying levels (*SI Appendix*, Fig. S1 *C* and *D*). This engineering pipeline enabled rapid generation of genetically encoded intrabodies as tools to dissect mTOR signaling and interaction networks (Fig. 1*B*).

To evaluate their utility as affinity reagents in Fab format, the cross-reactivity of these sABs with mTOR^{FRB}/TOR^{FRB} domains from diverse model organisms was investigated. Due to the evolutionary conservation of mTOR in eukaryotes, all sABs displayed binding to mTOR^{FRB}/TOR^{FRB} from *Homo sapiens*, *Mus musculus*, and *Drosophila melanogaster* (Fig. 1*C*). Additionally, sAB–R3G9 and sAB–R3H8 exhibited detectable binding to TOR1^{FRB} from *Saccharomyces cerevisiae*, despite sharing only 54% sequence identity with human mTOR^{FRB}. Binding affinities were determined by surface plasmon resonance for these sABs against human mTOR^{FRB}, with K_D values ranging from 50 pM for the tightest binder, sAB–R3H8, to 3.3 nM for the weakest binder, sAB–R3G9 (Fig. 1*D* and *SI Appendix*, Fig. S2*A*).

Central to the goal of developing genetically encodable mTOR inhibitors was to determine whether the epitopes engaged by these sABs overlap with the mTOR^{FRB} substrate recruitment site. Since endogenous mTORC1 substrates bind weakly to mTOR^{FRB}, FKBP12–Rapamycin was used as a surrogate competitor due to its favorable interaction with mTOR^{FRB}. Competitive single-point and multipoint ELISA assessed sAB binding to mTOR^{FRB} in the presence or absence of 10 μM FKBP12–Rapamycin. This competitive screening indicated that all tested sABs engage the mTOR^{FRB} substrate recruitment site (Fig. 1 *E*–*G* and *SI Appendix*, Fig. S2*B*). These results led to the selection of sAB–R3E9 and sAB–R3H8 as primary candidates for further development based on affinity and intracellular expression considerations.

Residual sAB binding signals in the presence of a competitor prompted an investigation into whether the sAB and FKBP12–Rapamycin epitopes are partially or fully overlapped. An in vitro fluorescence-based pulldown assay was developed based on rapamycin-induced ternary complex formation of FKBP12 and mTOR^{FRB} to validate obstruction of the mTOR^{FRB} substrate recruitment site (*SI Appendix*, Fig. S3 *A* and *B*). By titrating sAB–R3E9 or sAB–R3H8 into a mixture containing 10 nM biotinylated mTOR^{FRB}, 10 nM Alexa488-labeled SNAP–FKBP12, and 10 nM rapamycin, complete dose-dependent depletion of Alexa488–SNAP–FKBP12 was observed in streptavidin bead enrichment of biotinylated mTOR^{FRB} (*SI Appendix*, Fig. S3*C*). The IC_{50} values for sAB–R3E9 and sAB–R3H8 were determined to be 6.3 nM and 7.2 nM, respectively, for inhibiting the FKBP12–Rapamycin interaction with mTOR^{FRB} (Fig. 1 *H* and *I*). Furthermore, rapamycin-sensitive mTOR engagement and coordination of mTORC1 were confirmed by immunoprecipitation from human Expi293F cells treated with rapamycin or a vehicle control (Fig. 1 *J* and *K*). Finally, HeLa cells were immunostained with sAB–R3E9 and an anti-LAMP1 antibody, visually confirming lysosomal mTORC1 localization alongside other cellular locations, including the nucleus (*SI Appendix*, Fig. S4).

Crystal Structures of sAB–R3E9 and sAB–R3H8 Bound to mTOR^{FRB} Reveal mTORC1 Substrate Mimicry. To elucidate the structural features underlying sAB recognition of the mTOR^{FRB} substrate recruitment site, independent crystal structures of sAB–R3E9 and sAB–R3H8 bound to mTOR^{FRB} were solved at 1.6 Å and 2.0 Å resolution, respectively (*SI Appendix*, Table S1). The coordination of mTOR^{FRB} by sAB–R3E9 and sAB–R3H8 appeared highly similar, with differences primarily in the "elbow" angle connecting the CH1-CL and VH-VL domains (Fig. 2*A*). Extensive hydrogen bonding and Van der waals interactions along the relatively flat and hydrophobic substrate recruitment site provided the structural basis for the high binding affinities of

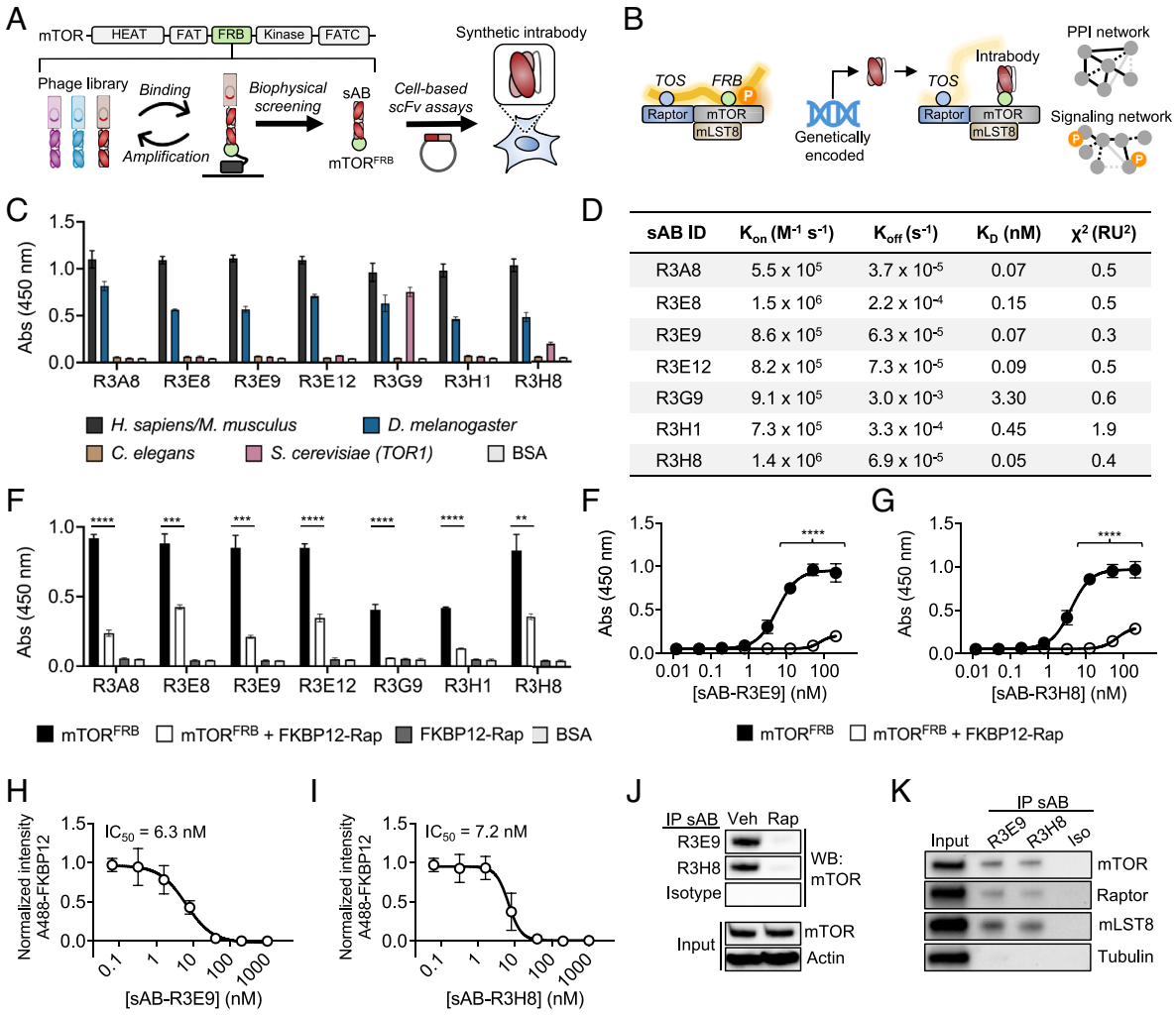

Fig. 1. Generating sABs against a key mTORC1 functional site. (*A*) Epitope-directed phage display biopanning strategy for generating mTOR^{FRB}-specific sABs and pipeline for scFv intrabody screening. (*B*) Model for genetically encoded intrabody-based modulation of the mTOR signaling network based on selective engagement of mTOR^{FRB}. (*C*) Single-point ELISA sAB cross-reactivity analysis using recombinant mTOR^{FRB} from the indicated model organisms (n = 3 independent replicates, mean ± SD). (*D*) Binding kinetics determined by SPR for unique sABs engineered against mTOR^{FRB}. (*E*) Competitive single-point ELISA reveals overlapping epitopes between all unique sABs and the mTOR^{FRB} (n = 3 independent replicates, mean ± SD. $^{**}P \le 0.01$, $^{***}P \le 0.001$, $^{****}P \le 0.0001$, unpaired *t* test). (*F*) Multipoint competitive ELISA screening for sAB–R3E9 and mTOR^{FRB} alone (black) or with 10 μM FKBP12–Rapamycin (white) in solution (n = 3 independent replicates, mean ± SD. $^{****}P \le 0.0001$, one-way ANOVA). (*G*) Multipoint competitive ELISA screening for sAB–R3H8 and mTOR^{FRB} alone (black) or with 10 μM FKBP12–rapamycin (white) in solution (n = 3 independent replicates, mean ± SD. $^{****}P \le 0.0001$, one-way ANOVA). (*H*) In vitro pulldown assay using 10 nM biotinylated SNAP-fused mTOR^{FRB} (Bio-mTOR^{FRB}), 10 nM Alexa488-labeled SNAP-fused FKBP12 (A488–FKBP12), 10 nM rapamycin, and varying concentrations of sAB–R3E9. Components were incubated for 30 min at room temperature before Bio-mTOR^{FRB} was enriched via streptavidin magnetic beads. A488–FKBP12 levels were monitored by SDS-PAGE (n = 3 independent replicates, mean ± SD). (*I*) In vitro pulldown assay using 10 nM biotinylated SNAP-fused mTOR^{FRB} (Bio-mTOR^{FRB}), 10 nM Alexa488-labeled SNAP-fused FKBP12 (A488–FKBP12), 10 nM rapamycin, and varying concentrations of sAB–R3H8. Components were incubated for 30 min at room temperature before Bio-mTOR^{FRB} was enriched via streptavidin magnetic beads. A488–FKBP12 levels were monitored by SDS-PAGE (n = 3 independent replicates, mean ± SD). (*J*) Representative immunoprecipitation-western blot analysis from Expi293F cells treated for 20 h with vehicle or 1 μM rapamycin. The indicated sABs were biotinylated through a C-terminal AviTag and added to lysates at 10 nM for 3 h with rotation at 4 °C before enrichment with streptavidin magnetic beads. (n = 3 biological replicates). (*K*) Representative immunoprecipitation-western blot analysis from Expi293F cells confirms that sAB–R3E9 and sAB–R3H8 can engage with and isolate mTORC1. The indicated sABs were biotinylated through a C-terminal AviTag and added to lysates at 50 nM for 3 h with rotation at 4 °C before enrichment with streptavidin magnetic beads. (n = 3 biological replicates).

70 pM and 50 pM for sAB–R3E9 and sAB–R3H8, respectively (*SI Appendix*, Fig. S5*A*). In agreement with binding assays, the paratopes of sAB–R3E9 and sAB–R3H8 are positioned to directly cover the FRB interface, interacting with nearly every mTOR^{FRB} residue that FKBP12–Rapamycin engages (*SI Appendix*, Fig. S5*B*). Alignment of the crystal structures of sAB–R3E9–mTOR^{FRB} and sAB–R3H8–mTOR^{FRB} with a previously determined cryo-EM structure of mTORC1 (PDB: 6BCX) confirmed that scFv-format binding is accessible to mTOR^{FRB}, with similar binding poses as S6K1$^{392\text{-}410}$ (PDB: 5WBH) and FKBP12–Rapamycin (PDB: 1FAP), illustrating their potential to obstruct substrate entry into the catalytic cleft (Fig. 2*B*).

Given these observations, an investigation was conducted to determine whether sAB–R3E9 and sAB–R3H8 share molecular recognition features with structurally characterized mTOR^{FRB}-dependent mTORC1 substrates. Multiple sequence alignment of mTOR^{FRB} showed that many residues contacted by these sABs are evolutionarily conserved from yeast to humans (*SI Appendix*, Fig. S5*C*). A quantitative analysis revealed solvent accessible surface area (SASA) burial of 1,148 Å^2 and 1,228 Å^2 by sAB–R3E9 and sAB–R3H8 with mTOR^{FRB}, respectively (Fig. 2*C*). These SASA values are significantly greater than those for S6K1$^{392\text{-}410}$, PRAS40$^{212\text{-}232}$, or FKBP12–Rapamycin, representing a favorable attribute toward obstruction of the substrate

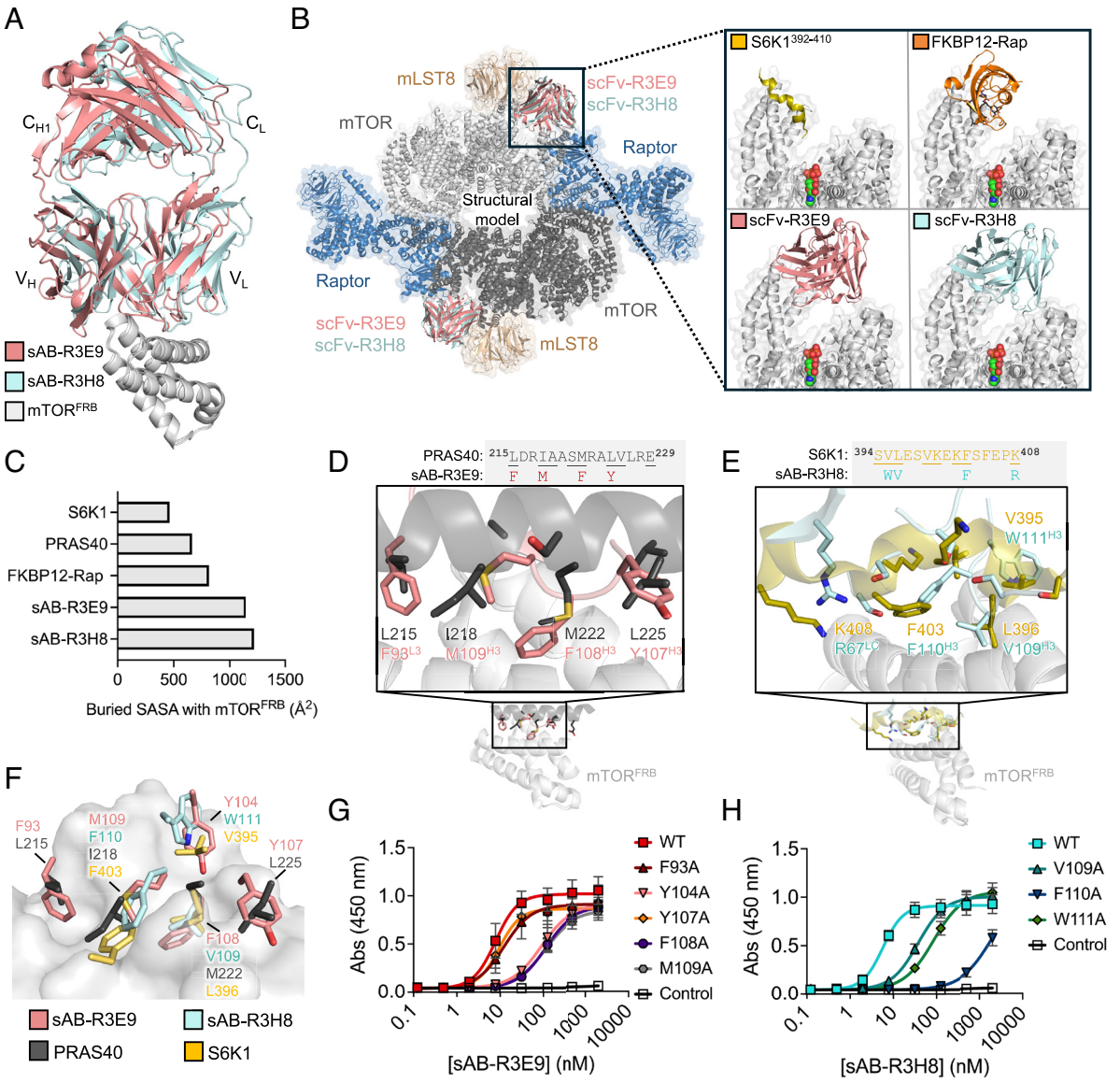

Fig. 2. Structural features of sABs engaged with the mTOR^{FRB} substrate recruitment site. (*A*) Alignment of crystal structures for sAB–R3E9 (salmon) and sAB–R3H8 (pale cyan) bound to mTOR^{FRB}. (*B*, *Left*) Structural model of sAB–R3E9 and sAB–R3H8 in scFv format aligned with a previously published cryo-EM structure of mTORC1 (PDB: 6BCX). (*Right*) Close-up view of mTOR^{FRB} and the active site (gray; ATP colored and shown as spheres) aligned with crystal structures of the S6K1$^{392-410}$–mTOR^{FRB} complex (yellow, PDB: 5WBH), FKBP12–Rapamycin–mTOR^{FRB} complex (orange, PDB: 1FAP), sAB–R3E9–mTOR^{FRB} (salmon, scFv format), and sAB–R3H8–mTOR^{FRB} (pale cyan, scFv format). (*C*) Quantification of buried solvent accessible surface area between mTOR^{FRB} and the indicated molecules. (*D*) Structural alignment of the endogenous mTOR inhibitor PRAS40 (dark gray, PDB: 5WBU) and sAB–R3E9 (salmon) interactions with mTOR^{FRB} (light gray). Underlined amino acids indicate direct PRAS40–mTOR^{FRB} interactions. sAB–R3E9 residues that contact the same site are listed below PRAS40 residues. (*E*) Structural alignment of the endogenous mTOR substrate S6K1 (yellow, PDB: 5WBH) and sAB–R3H8 (pale cyan) interactions with mTOR^{FRB} (light gray). Underlined amino acids indicate direct S6K1–mTOR^{FRB} interactions. sAB–R3H8 residues that contact the same site are listed below S6K1 residues. (*F*) Consensus hydrophobic interaction sites among endogenous (S6K1, PDB: 5WBH and PRAS40, PDB: 5WBU) and synthetic (sAB–R3E9 and sAB–R3H8) structurally characterized mTOR^{FRB} interacting proteins. (*G*) Multipoint ELISA for point mutations made in sAB–R3E9 at consensus interaction sites. (n = 3 independent experiments, mean ± SD). (*H*) Multipoint ELISA for point mutations made in sAB–R3H8 at consensus interaction sites. (n = 3 independent experiments, mean ± SD).

recruitment site. Examination of structural interactions revealed remarkable alignment between residues L215, I218, M222, and L225 from PRAS40$^{212-232}$ and residues F93^{L3}, Y107^{H3}, F108^{H3}, and M109^{H3} from sAB–R3E9 (Fig. 2*D*). Similarly, coordination between residues V395, L396, F403, and K408 from S6K1$^{392-410}$ and residues R67^{LC}, V109^{H3}, F110^{H3}, and W111^{H3} from sAB–R3H8 was observed (Fig. 2*E*).

Overall, five highly conserved positions of hydrophobic residue coordination at the mTOR^{FRB} substrate recruitment site were identified among naturally occurring or synthetic molecules despite entirely different sequence and secondary structure characteristics (Fig. 2*F*). Alanine scanning mutagenesis revealed significant energetic contributions (EC_{50} fold change > fivefold) toward mTOR^{FRB} binding by residues Y104^{H3}, F108^{H3}, and M109^{H3} in sAB–R3E9 and by residues V109^{H3}, F110^{H3}, and W111^{H3} in sAB–R3H8 (Fig. 1 *G* and *H* and *SI Appendix*, Fig. S6 *A* and *B*). These residues form a confined network at the center of the mTOR^{FRB} substrate recruitment site with almost no positional sequence identity between molecules. Together, crystal structure determination of two unique sABs bound to mTOR^{FRB} paired with structure-guided mutational binding assays provided molecular insight into the regulation of mTOR^{FRB}-dependent substrate recruitment. The findings suggest that mTOR^{FRB}-mediated coordination of mTORC1 substrates may be based primarily on a code of shape complementarity with low stringency for hydrophobic side chain stereochemistry at each position.

Conformation-Specific Intrabodies Highlight mTOR^{FRB} as an Allosteric Toggle Switch to Modulate the mTORC1 Architecture. Motivated by observations of molecular mimicry between sABs and mTORC1 substrates, the potential for sAB–R3E9 and sAB–R3H8 to engage with mTORC1 within human cells as intrabodies was explored. These intrabodies, termed Ib-R3E9 and Ib-R3H8, were confirmed to engage intracellularly with mTORC1 through transfection experiments in Expi293F cells. Cells were transfected with a FLAG-tagged isotype control intrabody (Ib-Iso), Ib-R3E9, or Ib-R3H8 for 48 h followed by anti-FLAG immunoprecipitation. Both Ib-R3E9 and Ib-R3H8 successfully pulled down mTOR and core mTORC1 components, such as mLST8 and Raptor, indicating that intrabody target engagement was maintained in the reducing intracellular environment (Fig. 3*A*). Interestingly, a significant decrease in Raptor signal was observed in the Ib-R3H8 pulldown compared to Ib-R3E9, while signals for mTOR and mLST8 remained consistent between these intrabodies (Fig. 3 *B*–*D*). This suggests that intrabody expression variability does not account for the difference in coimmunoprecipitated levels of Raptor. Instead, intracellular engagement of mTORC1 by Ib-R3E9 and Ib-R3H8 differentially influences the stability of the mTOR–Raptor interaction despite targeting nearly identical mTOR^{FRB} epitopes (Fig. 3 *E* and *F*). This effect could not be replicated by pan-mTOR immunoprecipitation from cell lysates spiked with biotinylated sAB–R3E9 or sAB–R3H8, indicating that modulation of the mTOR–Raptor interaction by Ib-R3E9 or Ib-R3H8 is dependent on a native, active intracellular environment (*SI Appendix*, Fig. S7).

The effects of intrabodies were compared to rapamycin to further understand how Ib-R3E9 and Ib-R3H8 modulate endogenous mTOR assemblies in cells. A pan-mTOR coimmunoprecipitation was performed in vehicle-treated cells, rapamycin-treated cells, and cells expressing FLAG-T2A and enhanced green fluorescent protein (eGFP) tagged Ib-Iso, Ib-R3E9, or Ib-R3H8 isolated by fluorescence-activated cell sorting (FACS). Consistent with previous reports, rapamycin treatment for 24 h markedly diminished interactions of both Raptor and Rictor with mTOR (Fig. 3*G*). The mTOR–Rictor interaction was obstructed similarly by both intrabodies, confirming that masking the mTOR^{FRB} substrate recruitment site is sufficient to obstruct the assembly of Rictor onto newly synthesized mTORC2 complexes. In contrast, distinctive stabilizing or destabilizing effects on the mTOR–Raptor interaction were observed between cells expressing Ib-R3E9 or Ib-R3H8, respectively.

Allosteric destabilization of the mTOR–Raptor interaction by Ib-R3H8 but not by Ib-R3E9 suggests that engagement of the FRB site alone is insufficient to induce Raptor dissociation. The structural mechanism underlying intrabody-based modulation of the mTOR–Raptor interaction was elucidated by examining interactions at the mTOR^{FRB} interface. Rapamycin, sAB–R3E9, and sAB–R3H8 exhibit similar structural arrangements when bound to mTOR^{FRB} (*SI Appendix*, Fig. S8 *A*–*C*). However, their epitopes are distinguished by altered surface topology in hydrophobic groove 1 (HG1) and 2 (HG2), particularly in the sAB–R3E9 bound state (*SI Appendix*, Fig. S8 *D*–*F*). HG1 morphology is characterized by rotation of the W2101 side chain while HG2 exhibits displacement of V2095 and Y2038 side chains, which are both coupled to shifts in the helical conformation of mTOR^{FRB} (*SI Appendix*, Fig. S8 *G*–*I*). Well-defined electron density shows a hydrogen bonding interaction between NE1 of W2101 and the hydroxyl of S2035 in HG1 of mTOR^{FRB} bound by sAB–R3E9. Notably, the hydrogen bonding geometry requires both these sidechains to adopt unfavorable rotamer dihedral angles (Fig. 3 *H* and *I*). The stabilization of this high-energy configuration is probably influenced not only by the hydrogen bonding interaction but also by a nest of five aromatic residues that form a π-stacking network between sAB–R3E9 (F93^{L3} and F108^{H3}) and mTOR^{FRB} (F2039, W2101, and F2108) (Fig. 3*J*). In other mTOR^{FRB} structures bound by sAB–R3H8, S6K1$^{392\text{-}410}$, PRAS40$^{212\text{-}232}$, or FKBP12–Rapamycin, W2101 and S2035 do not interact and are found in favorable, low-energy conformations (Fig. 3*K* and *SI Appendix*, Fig. S9).

To determine whether sAB side chain stereochemistry alone influences the coordination of mTOR^{FRB}, an anti-FLAG immunoprecipitation was performed using variants Ib-R3E9^{F108V} and Ib-R3H8^{V109F}. The results suggested that swapping side chain properties in the HG1 cavity is insufficient to influence the mTOR–Raptor interaction and that the phenylalanine introduced in Ib-R3H8^{V109F} sterically clashes with the low-energy W2101 rotamer in HG1 (*SI Appendix*, Fig. S10 *A*–*C*). Consequently, intrabody-based allosteric tunability of the mTOR–Raptor interaction appears to rely on discrimination for high-energy side chain conformations coupled to subtle rearrangements in mTOR^{FRB} helices α3 (1.6 Å, ~10°) and α4 (1.2 Å, ~7°) (Fig. 3 *L* and *M*). Our findings support a model where minor distortions in mTOR^{FRB} conformation can allosterically stabilize or destabilize the interaction between mTOR and Raptor. Future studies should explore whether distinct conformational states of mTOR^{FRB} have functional implications for regulating nutrient-dependent mTOR activity, complex assembly, or substrate coordination.

Ib-R3E9 and Ib-R3H8 Potently Inhibit mTOR Signaling in Human Cells. A FACS-based screening approach was utilized to test the hypothesis that engagement of the mTOR^{FRB} substrate recruitment site by intrabodies results in inhibition of mTOR^{FRB}-dependent mTORC1 signaling. Expression of eGFP-tagged intrabodies was observed to be cell-wide, suggesting that these binders are capable of engaging and inhibiting all pools of mTOR (*SI Appendix*, Fig. S11*A*). Western blotting was used to analyze phosphorylation levels of critical mTOR substrates in total Expi293F cell lysates from vehicle-treated cells, rapamycin-treated cells, and FACS-eGFP(+) cells expressing Ib-Iso, Ib-R3E9, or Ib-R3H8 (Fig. 4*A*). Both Ib-R3E9 and Ib-R3H8 effectively inhibited mTORC1-mediated phosphorylation of the rapamycin-sensitive S6K1^{T389} site without altering total mTOR or Raptor levels (Fig. 4 *B* and *C* and *SI Appendix*, Fig. S11*B*).

Intrabody-mediated effects on mTORC1 and mTORC2 signaling were further investigated over different time scales by comparing them to rapamycin treatment. Ib-R3E9 robustly inhibited mTORC1-mediated phosphorylation of S6K1^{T389} after both 24 and 48 h. In contrast, mTORC2-mediated phosphorylation of Akt^{S473} was only minimally suppressed after 24 h but more prominently after 48 h (Fig. 4 *D*–*F*). This pattern mirrored the time course observed in rapamycin-treated cells (*SI Appendix*, Fig. S12 *A*–*C*). While accurate time scales of intrabody-based inhibition warrant further study, this was not feasible with the transfection-based screening approach used here.

Confocal microscopy was employed to visually inspect immunostained ribosomal protein S6$^{S240/244}$ phosphorylation levels as a reporter of mTORC1 inhibition in HeLa cells expressing eGFP-tagged Ib-Iso, Ib-R3E9, and Ib-R3H8. Intrabody-based mTORC1 inhibition efficacy was supported by the ablation of S6$^{S240/244}$ phosphorylation levels in cells transfected with Ib-R3E9 and Ib-R3H8 compared to the negative control Ib-Iso (Fig. 4*G*). These results underscore the capability of synthetic intrabodies to effectively inhibit mTORC1 and mTORC2 signaling in a genetically encoded manner similar to rapamycin-based inhibition (Fig. 4*H*).

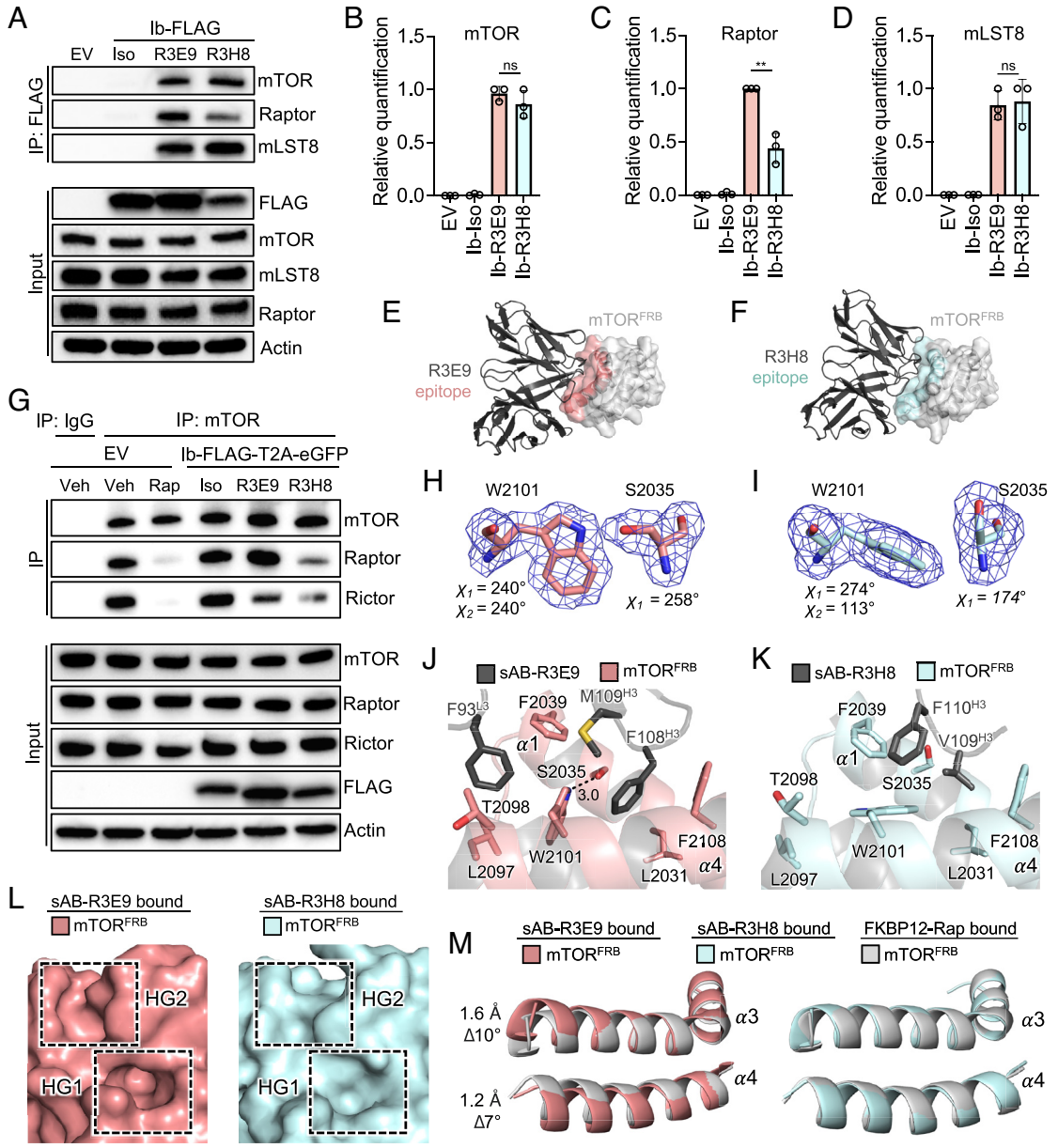

Fig. 3. Intrabody-based allosteric modulation of the mTOR–Raptor interaction. (*A*) Representative immunoprecipitation-western blot analysis of Expi293F cells transfected with empty vector (EV), isotype control (Iso), R3E9, or R3H8 FLAG-tagged intrabodies (Ib-FLAG) for 48 h. (*B*) Quantification of mTOR enrichment from the FLAG immunoprecipitation relative to input shown in *A*. (n = 3 biological replicates, mean ± SD. ns = not significant, unpaired *t* test). (*C*) Quantification of Raptor enrichment from the FLAG immunoprecipitation relative to input shown in *A*. (n = 3 biological replicates, mean ± SD. $^{**}P \leq 0.01$, unpaired *t* test). (*D*) Quantification of mLST8 enrichment from the FLAG immunoprecipitation relative to input shown in *A*. (n = 3 biological replicates, mean ± SD. ns = not significant, unpaired *t* test). (*E*) Structure of sAB–R3E9 (dark gray) in single-chain variable fragment format with its epitope (salmon) illustrated on mTOR^{FRB} (light gray). (*F*) Structure of sAB–R3H8 (dark gray) in single-chain variable fragment format with its epitope (pale cyan) illustrated on mTOR^{FRB} (light gray). (*G*) Representative immunoprecipitation-western blot analysis for intrabody-based modulation of mTOR–Raptor and mTOR–Rictor interactions. Expi293F cells were transfected with EV, isotype control (Iso), R3E9, or R3H8 FLAG-T2A-eGFP tagged intrabodies (Ib-FLAG-T2A-eGFP) for 24 h before isolation of eGFP(+) cells by FACS. Vehicle or 200 nM rapamycin were incubated with the indicated cells for 24 h. Samples were then lysed and subjected to pan-mTOR immunoprecipitation for analysis of protein–protein interactions (n = 3 biological replicates). (*H*) 2mFo-DFc electron density map (1σ contour) after refinement for W2101 and S2035 of mTOR^{FRB} in the sAB–R3E9 bound state. (*I*) 2mFo-DFc electron density map (1σ contour) after refinement for W2101 and S2035 of mTOR^{FRB} in the sAB–R3H8 bound state. (*J*) sAB–R3E9 interactions (dark gray) in hydrophobic groove 1 (HG1) and 2 (HG2) of mTOR^{FRB} (salmon) illustrates stabilization of W2101 and S2035 side chains in unfavorable rotameric states. An extensive π-stacking network is formed between F93^{L3} and F108^{H3} of sAB–R3E9 and F2039, W2101, and F2108 of mTOR^{FRB}. (*K*) sAB–R3H8 interactions (dark gray) in hydrophobic groove 1 (HG1) and 2 (HG2) of mTOR^{FRB} (pale cyan) illustrates favorable conformations of W2101 and S2035 side chains. (*L*) Surface representation of mTOR^{FRB} hydrophobic groove 1 (HG1) and 2 (HG2) topology from structures bound by sAB–R3E9 and sAB–R3H8. (*M*) Alignment of α3 and α4 helices from mTOR^{FRB} in the R3E9 bound state (salmon), R3H8 bound state (pale cyan), and previously published FKBP12–Rapamycin bound state (PDB: 1NSG; light gray). Binding of sAB–R3E9 triggers subtle changes in the configuration of α3 and α4 helices compared to sAB–R3H8 or FKBP12–Rapamycin.

Programmable Subcellular Intrabody Localization Enables Spatially Restricted Inhibition of mTOR in the Nucleus or Cytosol. While small-molecule inhibitors and genetic knockdown approaches have been invaluable for gaining general mechanistic insights into mTOR function, a platform was developed to perturb mTOR activity with subcellular spatial resolution. With structural and functional data supporting the efficacy of intrabody-based mTOR inhibition, Ib-R3E9 and Ib-R3H8 were modified by incorporating various subcellular localization tags (*SI Appendix*, Fig. S13*A*). Transfection of Ib-R3E9-eGFP equipped with tags such as nuclear export signal (NES), nuclear localization signal (NLS), Lyn kinase motif, or Yxxϕ motif in HeLa cells demonstrated

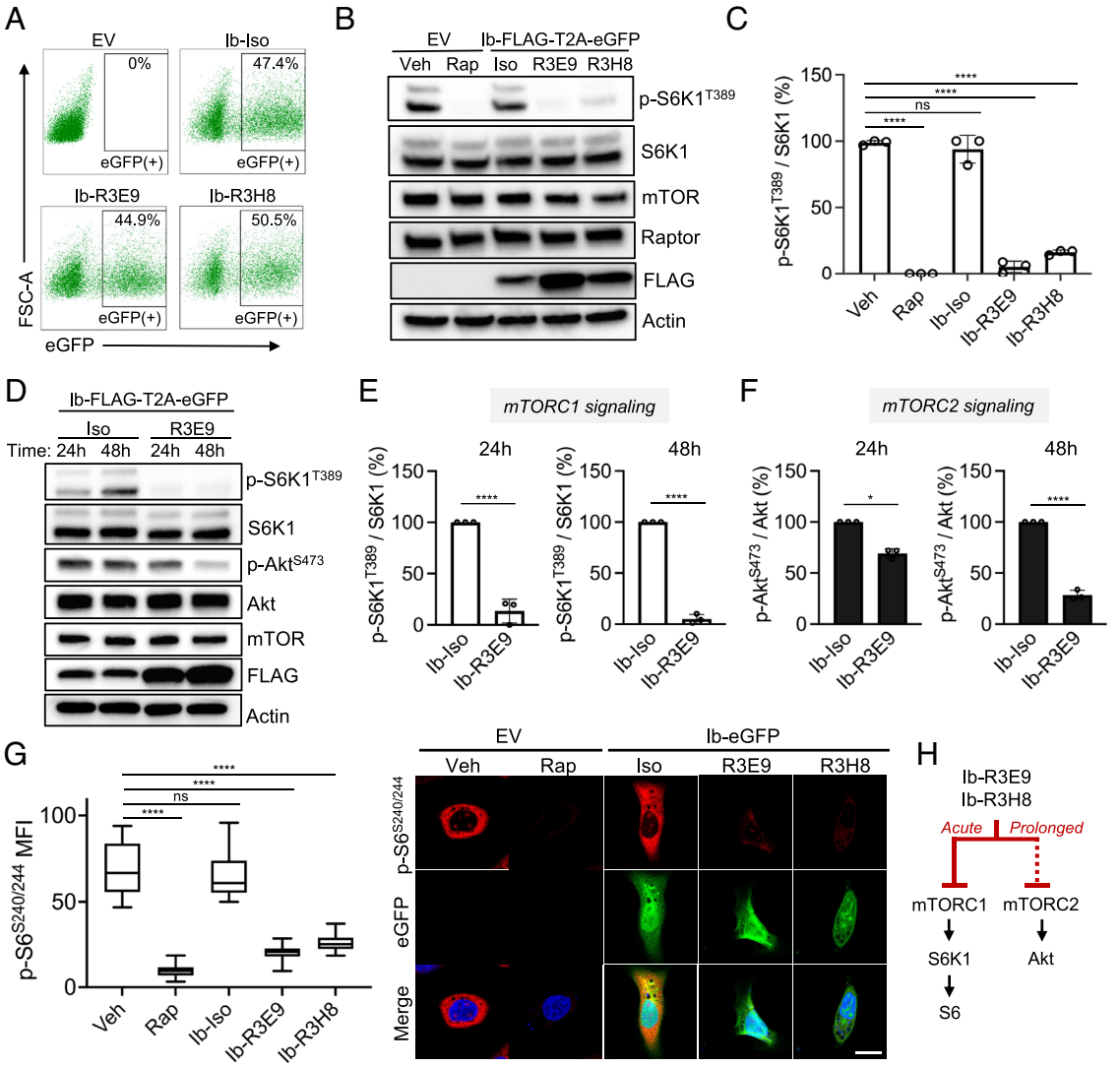

Fig. 4. Genetically encoded inhibition of mTOR signaling with synthetic intrabodies in human cells. (*A*) Representative FACS isolation of Expi293F cells transfected with EV, Iso, R3E9, or R3H8 FLAG-T2A-eGFP tagged intrabodies (Ib-FLAG-T2A-eGFP) for 24 h. (*B*) Representative western blot analysis of Expi293F cells transfected with EV, Iso, R3E9, or R3H8 FLAG-T2A-eGFP tagged intrabodies (Ib-FLAG-T2A-eGFP) for 24 h before isolation of eGFP(+) cells by FACS. EV cells were treated with vehicle and 100 nM rapamycin for 16 h as controls. (*C*) Quantification of relative p-S6K1^{T389} levels from the experiment in *B* (n = 3 biological replicates, mean ± SD. ns = not significant, ****$P \le 0.0001$, one-way ANOVA). (*D*) Representative western blot analysis of Expi293F cells transfected with the indicated constructs after 24-h and 48-h time points before isolation of eGFP(+) cells by FACS. (*E*) Quantification of relative p-S6K1^{T389} levels from the experiment in *D* (n = 3 biological replicates, mean ± SD. ****$P \le 0.0001$, one-way ANOVA). (*F*) Quantification of relative p-Akt^{S473} levels from the experiment in *D* (n = 3 biological replicates, mean ± SD. *$P \le 0.01$, ****$P \le 0.0001$, one-way ANOVA). (*G*, *Left*) Quantification of immunostained p-S6$^{S240/244}$ levels from the experiment in *H* (n = 19, 18, 21, 27, and 25 cells. ns = not significant, ****$P \le 0.0001$, one-way ANOVA with Tukey–Kramer test). (*Right*) Representative immunofluorescent confocal microscopy analysis of eGFP-tagged intrabody expression and of p-S6$^{S240/244}$ levels in HeLa cells. Scale bar denotes 20.5 μm. (n = 2 independent experiments). (*H*) Schematic of differential mTORC1 and mTORC2 inhibition by Ib-R3E9 and Ib-R3H8 as determined by intracellular functional assays.

the feasibility of directing synthetic intrabody inhibitors to specific locations within living cells (Fig. 5*A*).

The potential link between nuclear mTOR activity and distinct biological outputs is controversial due to the lack of tools for subcellular location-specific mTOR perturbations. Restricting intrabody residence to the cytosol or nucleus was envisioned as a means to selectively manipulate nuclear mTOR signaling separately from cytosolic mTOR signaling (Fig. 5*B*). To determine whether nucleus-restricted intrabodies could selectively perturb nuclear mTOR signaling, the canonical mTORC1 substrate S6K1 was tagged with N-terminal histone 2A (H2A) and mCherry (mChe) for stringent nuclear anchoring as a readout for nuclear mTOR activity as previously described (29). Confocal microscopy of HeLa cells cotransfected with H2A-mChe-S6K1 and Ib-R3E9-eGFP-NLSx2 or Ib-R3H8-eGFP-NLSx2 showed clear nuclear colocalization for each construct (Fig. 5*C* and *SI Appendix*, Fig. S13*B*). Western blot analysis confirmed successful perturbation of nuclear mTOR activity, as indicated by phosphorylation of exogenous H2A-mChe-S6K1^{T389}, which was ablated by rapamycin treatment and expression of Ib-R3E9-eGFP-NLSx2 or Ib-R3H8-eGFP-NLSx2 (Fig. 5*D*). Importantly, expression of nucleus-restricted intrabodies did not inhibit phosphorylation of endogenous S6K1^{T389}, which served as a cytosolic control since it is not found at appreciable levels in the nucleus (Fig. 5*E*).

As an orthogonal validation, immunostained S6$^{S240/244}$ phosphorylation was visualized as a reporter of the endogenous mTORC1 signaling network in response to cytosol-restricted or nucleus-restricted intrabody localization. S6$^{S240/244}$ phosphorylation was predominantly cytosolic and was selectively ablated by expression of cytosolic Ib-R3E9-eGFP-NESx2 and Ib-R3H8-eGFP-NESx2 (Fig. 5*F*). In contrast, expression of nuclear Ib-R3E9-eGFP-NLSx2

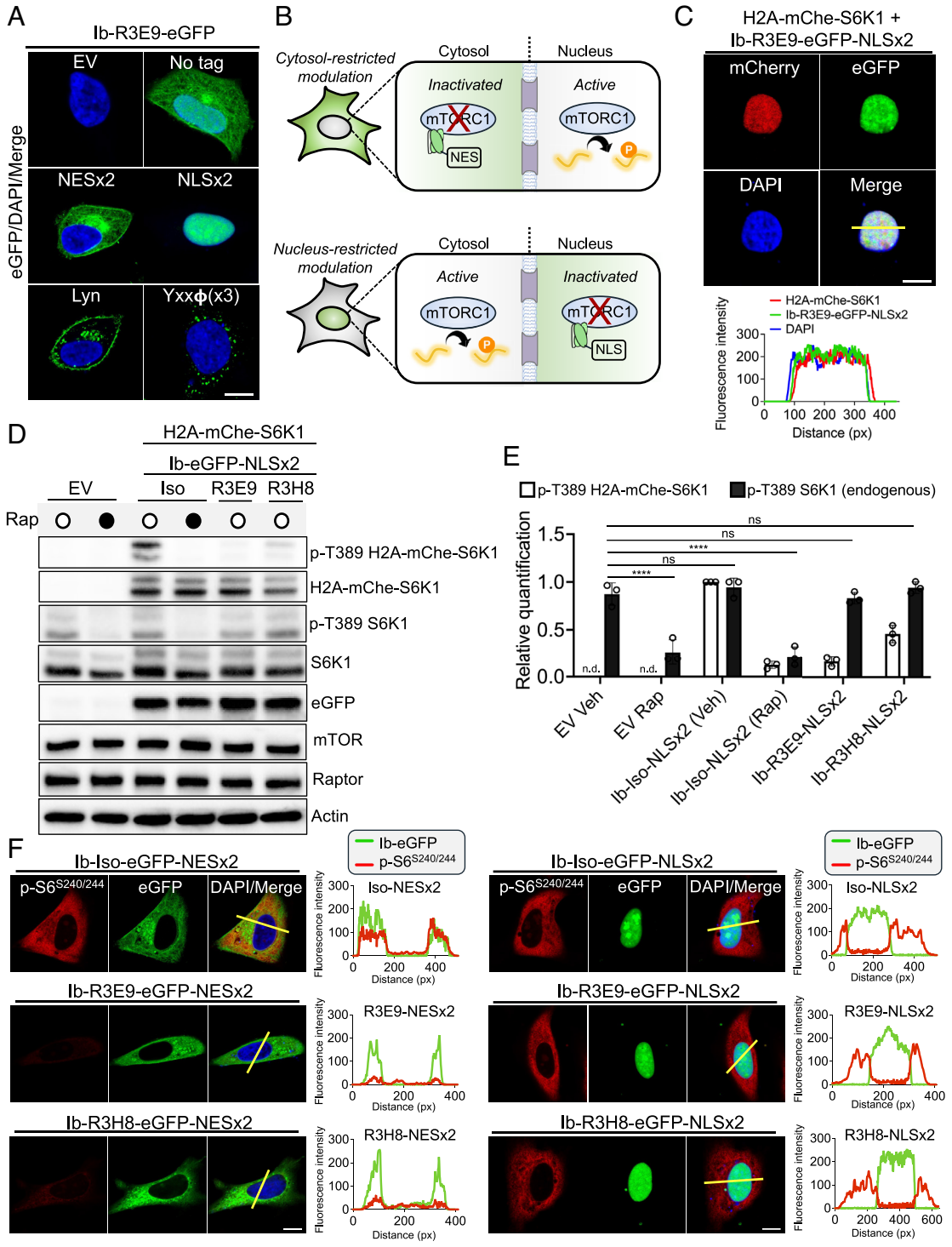

Fig. 5. Subcellular compartment-specific inhibition of the endogenous mTOR signaling network. (*A*) Representative confocal microscopy analysis of eGFP-tagged Ib-R3E9 with the indicated subcellular localization tags in HeLa cells. Scale bar denotes 11.5 μm. (*B*) Schematic of subcellular mTOR activity modulation assay using cytosol- or nucleus-restricted eGFP-tagged intrabodies bearing either NES or NLS tags, respectively. (*C, Top*) Representative confocal microscopy analysis of the nuclear colocalization between H2A-mCherry-S6K1 (red) and Ib-R3E9-eGFP-NLSx2 (green) in HeLa cells. Scale bar denotes 9.2 μm. (*Bottom*) Fluorescence profile along the yellow line traced in the merged image above. (*D*) Western blot analysis of HeLa cells transfected with EV controls or cotransfected with H2A-mCherry-S6K1 and Iso, R3E9, or R3H8 intrabodies bearing eGFP-NLSx2 tags for 48 h before treatment with vehicle or 500 nM rapamycin for 1 h. (*E*) Quantification of p-T389 H2A-mChe-S6K1 relative to total H2A-mChe-S6K1 and p-T389 S6K1 relative to actin from the experiment in *D*. Label of n.d. indicates no data collected for EV controls. (n = 3 biological replicates, mean ± SD. ns = not significant, ****$P \leq 0.0001$, one-way ANOVA). (*F*) Representative confocal microscopy analysis of endogenous mTOR signaling in HeLa cells transfected with eGFP-NESx2- or eGFP-NLSx2-tagged Iso, R3E9, or R3H8 intrabodies. Transfected cells were immunostained to determine endogenous levels of p-S6$^{S240/244}$ in the presence of cytosol- or nucleus-restricted intrabodies. Scale bar denotes 15.4 μm. Graphs on the right report fluorescence intensity profiles along the traced yellow lines shown in merged images. (n = 2 independent experiments).

and Ib-R3H8-eGFP-NLSx2 did not affect S6$^{S240/244}$ phosphorylation levels, confirming that mTORC1 signaling remained unaffected in regions disconnected from the compartmentalized intrabodies. These results demonstrate the versatility of a modular intrabody-based system capable of perturbing mTOR signaling at specific subcellular locations.

Discussion

Genetically encodable probes have become essential tools for identifying druggable targets within complex therapeutic pathways. Despite advancements in fluorescence-based mTOR activity reporters and chemical-genetic mTOR inhibition platforms (20, 27, 28, 53), these methods would benefit significantly from the precise spatial and temporal control of mTOR signaling at the subcellular level. To enable this, we developed genetically encodable synthetic binders for detailed analysis of subcellular mTOR signaling dynamics. We engineered versatile scFv-based intrabodies that obstruct an important substrate recruitment site and stabilize specific conformational states of mTOR by recognizing nearly identical epitopes. These intrabodies enable subcellular activity perturbations in the mTOR signaling network with high spatial resolution, offering an approach to explore the structural and location-specific intricacies of the mTOR pathway.

A more complete understanding of the recruitment and stabilization of mTORC1 substrates for phosphorylation is crucial for developing new therapeutic strategies. Our structure-guided mutational studies revealed significant similarities in how endogenous (e.g., S6K1 and PRAS40) and synthetic (e.g., sAB–R3E9 and sAB–R3H8) binding molecules recognize the $mTOR^{FRB}$ substrate recruitment site. Despite low sequence identity at consensus interaction sites, hydrophobic shape complementarity appears to be a key factor in substrate docking. The $mTOR^{FRB}$ site may also recruit other substrates like GRB10, TFEB, MAF1, and LIPIN through hydrophobic residues near phosphorylation sites (43). Understanding these interactions could provide insights into the molecular code of $mTOR^{FRB}$ substrate coordination. Additionally, it remains unclear whether nuclear mTORC1 substrates use this recruitment mechanism. Other mechanisms, such as TOS recruitment by Raptor, are vital for mTORC1 function. Developing intrabodies to block TOS–Raptor interactions will offer different ways to control mTOR function.

Engineered sABs are endowed with the ability to stabilize specific conformational states of their target antigens linked to biological functions. By combining high-resolution crystal structure analysis with cell-based functional assays, we gained insights into the allosteric regulation of mTORC1 architecture. Our results indicate that Ib-R3E9 and Ib-R3H8 stabilize distinct conformational states through coordination of the $mTOR^{FRB}$ substrate recruitment site. We identified a high-energy $mTOR^{FRB}$ conformation stabilized by sAB–R3E9 that is characterized by surface-exposed side chain reorientation and α-helix displacement. These observations suggest that $mTOR^{FRB}$ might act as a conformational switch to regulate mTORC1 stability. The relevance of these conformational changes to nutrient-dependent signaling or kinase activity remains to be answered.

We demonstrated effective rapamycin-like inhibition of mTOR by encoding Ib-R3E9 and Ib-R3H8 in human cell lines. This mode of inhibition is informative as it captures both therapeutic benefits and toxicities similar to rapamycin treatment. Notably, Ib-R3E9 showed near-complete inhibition of the rapamycin-sensitive p-S6K1^{T389} site, while Ib-R3H8 was slightly less potent, possibly due to lower intracellular solubility. This could be due to a tendency for aggregation, which is not uncommon for scFv-based intrabodies (54). We also found that cytosolic and nuclear mTOR networks could be independently manipulated by tagging Ib-R3E9 and Ib-R3H8 with NES or NLS sequences. This provides a basis for studying how subcellular origins of mTOR signaling relate to biological functions, such as in prostate cancer where hyperactivation reprograms transcription through downstream components (3).

While cell culture models offer insights into signal transduction pathways, they do not fully capture organismal cellular communication complexities. Although we have not encoded intrabodies in model organisms yet, they could potentially provide spatial and temporal control over in vivo mTOR/TOR signaling for tissue- or cell-specific studies. We demonstrated cross-reactivity with mTOR/TOR/TOR1 from various species using in vitro assays, suggesting that an epitope-directed engineering approach could yield selective binders for other model organisms. Overall, our intrabody-based platform should enable researchers to explore noncanonical mechanisms of subcellular mTOR signaling through systematic location-specific perturbations.

Methods

Detailed descriptions for procedures of molecular cloning, biophysical characterization, immunoprecipitation, and immunofluorescence are located in the *SI Appendix*.

Cell Culture and Transfections. Expi293F cells (Thermo Fisher Scientific) were cultured in Expi293 Expression Medium and handled according to the manufacturer's recommendations. Transfections in Expi293F were performed using the ExpiFectamine 293 Transfection Kit (Thermo Fisher Scientific) following the manufacturer's protocol for 24 to 48 h. The step of adding transfection enhancers 1 and 2 was disregarded here. HeLa cells (ATCC) were cultured in Dulbecco's modified Eagle medium supplemented with 1% Pen-Strep (Gibco) and 10% fetal bovine serum. Transfections in HeLa were performed using Lipofectamine LTX Reagent with PLUS Reagent (Thermo Fisher Scientific) according to the manufacturer's protocol for 24 to 48 h.

FACS. Expi293F cells transiently expressing FLAG-T2A-eGFP tagged intrabodies for the indicated time points were passed through 40 μm cell strainers (Falcon) and sorted using the BigFoot Cell Sorter (2 to 4 million cells each) into prewarmed Expi293 Expression Medium. Untransfected Expi293F cells were used as a negative control to establish gates for sorting eGFP(+) cells. After sorting, cells were centrifuged at 200× g for 5 min, resuspended in prewarmed Expi293 Expression Medium, and cultured at 37 °C for 1 h before harvesting for immunoprecipitation or western blot analysis.

Protein Expression and Purification. Expression of SNAP-6xHis, SNAP-$mTOR^{FRB}$-6xHis, SNAP-FKBP12-6xHis, and $mTOR^{FRB}$ with N-terminal 10xHis and Tobacco Etch Virus (TEV) tags was performed using BL21(DE3) competent *E. coli*. Cells were grown in 2×YT medium to OD_{600} = 0.6 to 0.8, 1 mM isopropyl β-D-1-thiogalactopyranoside (IPTG) was added, and cells were incubated overnight at 20 °C before harvesting by centrifugation. Purification followed a previously described protocol (55). Removal of 10×His-tag was performed by incubated TEV protease with 10×His-TEV-$mTOR^{FRB}$ at 1:50 ratio (w/w) overnight at 4 °C in the presence of 0.5 μM Tris(2-carboxyethyl)phosphine hydrochloride (TCEP). Next day, samples were incubated with TALON resin (Takara Bio) for 1 h with rotation at 4 °C before collecting the flow through for purity analysis by sodium dodecyl sulfate-polyacrylamide gel electrophoresis (SDS-PAGE). Periplasmic expression of Fabs was performed in BL21 competent *Escherichia coli*. Cells were grown in 2×YT medium to OD_{600} = 0.6 to 0.8, 1 mM IPTG was added, and cells were incubated for 4 h at 37 °C before harvesting by centrifugation. Fab purification was performed as previously described (56). Fabs with AviTag were expressed in CVB101 cells following the same protocol above with the exception of adding 50 μM biotin at the time of induction.

Phage Display Selection. Phage display selection was performed as previously described (56). Prior to library sorting, SNAP-$mTOR^{FRB}$ was site-specifically biotinylated by incubation with SNAP-Biotin (NEB) in the presence of 0.3 mM TCEP for 30 min at 37 °C. Biotinylated SNAP-$mTOR^{FRB}$ (Bio-SNAP-$mTOR^{FRB}$) was immobilized onto Streptavidin MagneSphere Paramagnetic Particles (Promega) for five rounds of phage selection. In the first round, 1 μM of Bio-SNAP-$mTOR^{FRB}$ was immobilized on 200 μL streptavidin magnetic beads and was incubated with 1 mL phage library (10^{10} CFU) for 1 h at room temperature with gentle shaking. The beads were washed three times to remove nonspecific phage, added to log phase *E. coli* XL-1 blue cells (Stratagene), and incubated for 20

min at room temperature. Medium supplemented with 0.1 mg/mL ampicillin and M13K07 helper phage (NEB) was added for amplification overnight at 37 °C. The amplified phage was precipitated by adding 20% polyethylene glycol (PEG) 8000, 2.5 M NaCl at a 1:5 ratio for 20 min on ice. Before each round, the amplified phage pool underwent competitive and subtractive selection using nonbiotinylated SNAP-tag only and empty streptavidin paramagnetic beads for 30 min with shaking to eliminate nonspecific binders. The final antigen concentration was dropped systematically from 1 μM to 2 nM from the first to the fifth round (200 nM second round, 50 nM third round, 20 nM fourth round, and 2 nM fifth round). After phage binding, the beads were subjected to five washing rounds with 0.5% bovine serum albumin and phosphate buffered saline supplemented with Tween 20 (BSA/PBST). The bound phages were eluted using 0.1 M glycine, pH 2.6, and neutralized with TRIS-HCl, pH 8.5. Then, the phage eluate was used for *E. coli* infection and phage amplification, as described above. Additional selection pressure using 1 μM of nonbiotinylated SNAP-tag in all washes was applied to ensure specificity to mTOR^{FRB}. After the fourth and fifth rounds, the infected cells were plated on ampicillin agar, and 192 colonies were picked to produce phage clones for single-point phage ELISA. Clones demonstrating high specificity for mTOR^{FRB} were sequenced and reformatted into the RH2.2 expression vector.

Crystallization and Structure Determination. sAB–R3E9•mTOR^{FRB} and sAB–R3H8•mTOR^{FRB} complexes were purified in 10 mM 4-(2-Hydroxyethyl) piperazine-1-ethanesulfonic acid (HEPES), pH 7.2, 150 mM NaCl by size exclusion chromatography (SEC) using a Sephadex 200 column. Evaluation of SEC purity was performed by analyzing fractions via SDS-PAGE. Pure complexes were concentrated to at least 10 mg/mL for crystallization screening facilitated by the Mosquito Crystal Robot (TTP Labtech). Crystallization conditions for the sAB–R3E9•mTOR^{FRB} complex were 0.2 M Calcium chloride dihydrate, 16% PEG 3350. Crystals were soaked in reservoir solution containing 20% PEG 400 as a cryoprotectant before being flash frozen in liquid nitrogen. Crystallization conditions for the sAB–R3H8•mTOR^{FRB} complex were 0.1 M HEPES, pH 7.5, 4% PEG 400, 2.2 M ammonium sulfate. Crystals were directly flash-frozen in liquid nitrogen for data collection. X-ray diffraction datasets were collected at the 23-ID-D beamline of the Advanced Photon Source at Argonne National Laboratory. Molecular replacement was used to solve crystal structures of sAB–R3E9•mTOR^{FRB} and sAB–R3H8•mTOR^{FRB} using structures of FRB (PDB: 1FAP) and Fab (PDB: 6U8C) in Phaser-MR (57). Models were refined using phenix.refine (58) and manually built using Coot (59) over iterative alternating cycles. All structural figures were generated using PyMOL. Coordinates have been deposited to the Protein Data Bank (9DBO and 9DL0).

Data, Materials, and Software Availability. Structure coordinates data have been deposited in Protein Data Bank (9DL0 and 9DBO) (60, 61). All other data are included in the article and/or *SI Appendix*.

ACKNOWLEDGMENTS. We sincerely appreciate the helpful advice from Jinyang Li in regard to confocal microscopy imaging experiments. We would like to thank the University of Chicago Sanger DNA Sequencing Core for their services, University of Chicago Cytometry and Antibody Technology Facility for their assistance with fluorescence-activated cell sorting using the Bigfoot Cell Sorter (RRID: SCR_017760) and University of Chicago Integrated Light Microscopy Core where confocal imaging was performed (RRID: SCR_019197). We are grateful for the use of the crystallization robot from the laboratory of Joseph Piccirilli. X-ray diffraction data were acquired at the 23-ID-D beamline of the Advanced Photon Source at Argonne National Laboratory. GM/CA@APS has been funded by the National Cancer Institute (ACB-12002) and the National Institute of General Medical Sciences (AGM-12006, P30GM138396). This research used resources of the Advanced Photon Source, a U.S. Department of Energy (DOE) Office of Science User Facility operated for the DOE Office of Science by Argonne National Laboratory under Contract No. DE-AC02-06CH11357. The Eiger2 16M detector at GM/CA-XSD was funded by NIH grant S10OD03426. This work was supported by the NIH grant R01GM117372 (A.A.K.). K.M.O. was funded in part by NIH T32 GM144292.

1. R. A. Saxton, D. M. Sabatini, mTOR signaling in growth, metabolism, and disease. *Cell* **168**, 960–976 (2017).
2. J. J. Howell, B. D. Manning, mTOR couples cellular nutrient sensing to organismal metabolic homeostasis. *Trends Endocrinol. Metab.* **22**, 94–102 (2011).
3. É. Audet-Walsh *et al.*, Nuclear mTOR acts as a transcriptional integrator of the androgen signaling pathway in prostate cancer. *Genes Dev.* **31**, 1228–1242 (2017).
4. Y. Zhong, X. Zhou, K.-L. Guan, J. Zhang, Rheb regulates nuclear mTORC1 activity independent of farnesylation. *Cell Chem. Biol.* **29**, 1037–1045.e4 (2022).
5. D.-H. Kim *et al.*, mTOR interacts with raptor to form a nutrient-sensitive complex that signals to the cell growth machinery. *Cell* **110**, 163–175 (2002).
6. D. D. Sarbassov *et al.*, Rictor, a novel binding partner of mTOR, defines a rapamycin-insensitive and raptor-independent pathway that regulates the cytoskeleton. *Curr. Biol.* **14**, 1296–1302 (2004).
7. A. Jain *et al.*, Stoichiometry and assembly of mTOR complexes revealed by single-molecule pulldown. *Proc. Natl. Acad. Sci. U.S.A.* **111**, 17833–17838 (2014).
8. S. Battaglioni, D. Benjamin, M. Wälchli, T. Maier, M. N. Hall, mTOR substrate phosphorylation in growth control. *Cell* **185**, 1814–1836 (2022).
9. D. E. Harrison *et al.*, Rapamycin fed late in life extends lifespan in genetically heterogeneous mice. *Nature* **460**, 392–395 (2009).
10. A. V. Shindyapina *et al.*, Rapamycin treatment during development extends life span and health span of male mice and Daphnia magna. *Sci. Adv.* **8**, eabo5482 (2022).
11. P. Juricic *et al.*, Long-lasting geroprotection from brief rapamycin treatment in early adulthood by persistently increased intestinal autophagy. *Nat. Aging* **2**, 824–836 (2022).
12. J. M. Schinaman, A. Rana, W. W. Ja, R. I. Clark, D. W. Walker, Rapamycin modulates tissue aging and lifespan independently of the gut microbiota in Drosophila. *Sci. Rep.* **9**, 7824 (2019).
13. J. R. Roth *et al.*, Rapamycin reduces neuronal mutant huntingtin aggregation and ameliorates locomotor performance in Drosophila. *Front. Aging Neurosci.* **15** (2023).
14. S. Robida-Stubbs *et al.*, TOR signaling and rapamycin influence longevity by regulating SKN-1/Nrf and DAF-16/FoxO. *Cell Metab.* **15**, 713–724 (2012).
15. L. Willems *et al.*, The dual mTORC1 and mTORC2 inhibitor AZD8055 has anti-tumor activity in acute myeloid leukemia. *Leukemia* **26**, 1195–1202 (2012).
16. S.-Y. Sun, mTOR kinase inhibitors as potential cancer therapeutic drugs. *Cancer Lett.* **340**, 1–8 (2013).
17. K. E. O'Reilly *et al.*, mTOR inhibition induces upstream receptor tyrosine kinase signaling and activates Akt. *Cancer Res.* **66**, 1500–1508 (2006).
18. J. Liu *et al.*, Targeting the mTOR pathway in breast cancer. *Tumour Biol.* **39**, 1010428317710825 (2017).
19. S. A. Soefje, A. Karnad, A. J. Brenner, Common toxicities of mammalian target of rapamycin inhibitors. *Target Oncol.* **6**, 125–129 (2011).
20. D. R. Wassarman, K. Bankapalli, L. J. Pallanck, K. M. Shokat, Tissue-restricted inhibition of mTOR using chemical genetics. *Proc. Natl. Acad. Sci. U.S.A.* **119**, e2204083119 (2022).
21. Z. Zhang *et al.*, Brain-restricted mTOR inhibition with binary pharmacology. *Nature* **609**, 822–828 (2022).
22. D. Filer *et al.*, RNA polymerase III limits longevity downstream of TORC1. *Nature* **552**, 263–267 (2017).
23. V. Giguère, Canonical signaling and nuclear activity of mTOR: A teamwork effort to regulate metabolism and cell growth. *FEBS J.* **285**, 1572–1588 (2018).
24. C. Betz, M. N. Hall, Where is mTOR and what is it doing there? *J. Cell Biol.* **203**, 563–574 (2013).
25. J. M. Carosi, C. Fourrier, J. Bensalem, T. J. Sargeant, The mTOR–lysosome axis at the centre of ageing. *FEBS Open Bio.* **12**, 739–757 (2022).
26. K. B. Rogala *et al.*, Structural basis for the docking of mTORC1 on the lysosomal surface. *Science* **366**, 468–475 (2019).
27. X. Zhou *et al.*, Dynamic visualization of mTORC1 activity in living cells. *Cell Rep.* **10**, 1767–1777 (2015).
28. N. Bouquier *et al.*, AIMTOR, a BRET biosensor for live imaging, reveals subcellular mTOR signaling and dysfunctions. *BMC Biol.* **18**, 81 (2020).
29. X. Zhou *et al.*, Location-specific inhibition of Akt reveals regulation of mTORC1 activity in the nucleus. *Nat. Commun.* **11**, 6088 (2020).
30. C. K. Tsang, H. Liu, X. F. S. Zheng, mTOR binds to the promoters of RNA polymerase I- and III-transcribed genes. *Cell Cycle* **9**, 953–957 (2010).
31. T. Kantidakis, B. A. Ramsbottom, J. L. Birch, S. N. Dowding, R. J. White, mTOR associates with TFIIIC, is found at tRNA and 5S rRNA genes, and targets their repressor Maf1. *Proc. Natl. Acad. Sci. U.S.A.* **107**, 11823–11828 (2010).
32. C. R. Dufour *et al.*, The mTOR chromatin-bound interactome in prostate cancer. *Cell Rep.* **38**, 110534 (2022).
33. F. Artoni, N. Grützmacher, C. Demetriades, Unbiased evaluation of rapamycin's specificity as an mTOR inhibitor. *Aging Cell* **22**, e13888 (2023).
34. Y. Chen, L. Han, C. R. Dufour, A. Alfonso, V. Giguère, Canonical and nuclear mTOR specify distinct transcriptional programs in androgen-dependent prostate cancer cells. *Mol. Cancer Res.* **22**, 113–124 (2024).
35. E. S. Ali *et al.*, Recent advances and limitations of mTOR inhibitors in the treatment of cancer. *Cancer Cell Int.* **22**, 284 (2022).
36. B. Mao *et al.*, Overview of research into mTOR inhibitors. *Molecules* **27**, 5295 (2022).
37. J. Li, S. G. Kim, J. Blenis, Rapamycin: One drug, many effects. *Cell Metab.* **19**, 373–379 (2014).
38. J. Chen, X. F. Zheng, E. J. Brown, S. L. Schreiber, Identification of an 11-kDa FKBP12-rapamycin-binding domain within the 289-kDa FKBP12-rapamycin-associated protein and characterization of a critical serine residue. *Proc. Natl. Acad. Sci. U.S.A.* **92**, 4947–4951 (1995).
39. P. P. Hsu *et al.*, The mTOR-regulated phosphoproteome reveals a mechanism of mTORC1-mediated inhibition of growth factor signaling. *Science* **332**, 1317–1322 (2011).
40. S. A. Kang *et al.*, mTORC1 phosphorylation sites encode their sensitivity to starvation and rapamycin. *Science* **341**, 1236566 (2013).
41. C. Gaubitz *et al.*, Molecular basis of the rapamycin insensitivity of target of rapamycin complex 2. *Mol. Cell.* **58**, 977–988 (2015).
42. H. Yang *et al.*, mTOR kinase structure, mechanism and regulation. *Nature* **497**, 217–223 (2013).
43. H. Yang *et al.*, Mechanisms of mTORC1 activation by RHEB and inhibition by PRAS40. *Nature* **552**, 368–373 (2017).
44. A. Pini, L. Bracci, Phage display of antibody fragments. *Curr. Protein Pept. Sci.* **1**, 155–169 (2000).

45. M. Paduch *et al.*, Generating conformation-specific synthetic antibodies to trap proteins in selected functional states. *Methods* **60**, 3–14 (2013).
46. P. Akkapeddi *et al.*, Exploring switch II pocket conformation of KRAS(G12D) with mutant-selective monobody inhibitors. *Proc. Natl. Acad. Sci. U.S.A.* **120**, e2302485120 (2023).
47. A. Zorba *et al.*, Allosteric modulation of a human protein kinase with monobodies. *Proc. Natl. Acad. Sci. U.S.A.* **116**, 13937–13942 (2019).
48. M. Baidya *et al.*, Allosteric modulation of GPCR-induced β-arrestin trafficking and signaling by a synthetic intrabody. *Nat. Commun.* **13**, 4634 (2022).
49. E. Ghosh *et al.*, A synthetic intrabody-based selective and generic inhibitor of GPCR endocytosis. *Nat. Nanotechnol.* **12**, 1190–1198 (2017).
50. H. Farrants *et al.*, Chemogenetic control of nanobodies. *Nat. Methods* **17**, 279–282 (2020).
51. L. J. Bailey *et al.*, Locking the elbow: Improved antibody Fab fragments as chaperones for structure determination. *J. Mol. Biol.* **430**, 337–347 (2018).
52. M. Baidya *et al.*, Genetically encoded intrabody sensors report the interaction and trafficking of β-arrestin 1 upon activation of G-protein–coupled receptors. *J. Biol. Chem.* **295**, 10153–10167 (2020).
53. C. Li *et al.*, TORSEL, a 4EBP1-based mTORC1 live-cell sensor, reveals nutrient-sensing targeting by histone deacetylase inhibitors. *Cell Biosci.* **14**, 68 (2024).
54. H. Kabayama *et al.*, An ultra-stable cytoplasmic antibody engineered for in vivo applications. *Nat. Commun.* **11**, 336 (2020).
55. T. Slezak *et al.*, Engineered protein G variants for multifunctional antibody-based assemblies. *Protein Sci.* **34**, e70019 (2025).
56. T. Slezak, A. A. Kossiakoff, Engineered ultra-high affinity synthetic antibodies for SARS-CoV-2 neutralization and detection. *J. Mol. Biol.* **433**, 166956 (2021).
57. A. J. McCoy *et al.*, Phaser crystallographic software. *J. Appl. Crystallogr.* **40**, 658–674 (2007).
58. P. V. Afonine *et al.*, Towards automated crystallographic structure refinement with Phenix.refine. *Acta Crystallogr. D Biol. Crystallogr.* **68**, 352–367 (2012).
59. P. Emsley, K. Cowtan, Coot: Model-building tools for molecular graphics. *Acta Crystallogr. D Biol. Crystallogr.* **60**, 2126–2132 (2004).
60. K. M. O'Leary, T. Slezak, A. A. Kossiakoff, Crystal structure of a synthetic Fab (R3H8) in complex with the FRB domain of mTOR. Protein Data Bank. https://doi.org/10.2210/pdb9DL0/pdb. Deposited 7 October 2024.
61. K. M. O'Leary, T. Slezak, A. A. Kossiakoff, Crystal structure of a synthetic Fab (R3E9) in complex with the FRB domain of mTOR. Protein Data Bank. https://doi.org/10.2210/pdb9DBO/pdb. Deposited 23 September 2024.